

MIMIC: Multimodal Inversion for Model Interpretation and Conceptualization

Animesh Jain, Alexandros Stergiou
University of Twente, The Netherlands
a.jain-2@student.utwente.nl, a.g.stergiou@utwente.nl

Abstract—Vision Language Models (VLMs) encode multimodal inputs over large, complex, and difficult-to-interpret architectures, which limit transparency and trust. We propose a Multimodal Inversion for Model Interpretation and Conceptualization (MIMIC) framework to visualize the internal representations of VLMs by synthesizing visual concepts corresponding to internal encodings. MIMIC uses a joint VLM-based inversion and a feature alignment objective to account for VLM’s autoregressive processing. It additionally includes a triplet of regularizers for spatial alignment, natural image smoothness, and semantic realism. We quantitatively and qualitatively evaluate MIMIC by inverting visual concepts over a range of varying-length free-form VLM output texts. Reported results include both standard visual quality metrics as well as semantic text-based metrics. To the best of our knowledge, this is the first model inversion approach addressing visual interpretations of VLM concepts.

Project page: <https://anaekin.github.io/MIMIC>

Index Terms—Model Inversion, Image Reconstruction, Model Interpretability, Concept Visualization, Feature Attribution

I. INTRODUCTION

Vision-Language Models (VLMs) have demonstrated impressive capabilities in numerous tasks. Despite their ability to compositionally encode multiple modalities with complex architectures, their transparency and interpretability remain limited due to their entangled representations. Interpreting internal encodings helps assess whether models genuinely reason [1–3] or interpolate from memorized examples [4, 5].

Given that each iteration of deep models increases complexity [6], uncovering visual explanations for their decisions has been a central point for research. Methods have focused on visualizing image region attributions [7, 8], attention patterns and hidden activations [9], tracing information flow, or editing representations in LLMs [3, 5, 10, 11]. These methods, however, are primarily unimodal and rely on gradient access, auxiliary decoders, or architecture-specific modifications.

In this paper, we address this interpretability gap by synthesizing visualizations of internal VLM representations with a Multimodal Inversion for Model Interpretation and Conceptualization (MIMIC) framework. MIMIC extends current unimodal inversion methods to autoregressive multimodal models to visualize their feature space. During training, we use an adversarial prompt to supervise the synthesis objective from the model’s generated answer. We additionally include a guidance objective to align the mean and variance of intermediate encodings with those computed from real images. Additional regularization terms promote spatial smoothness, consistency across patches, and alignment with natural image distributions.

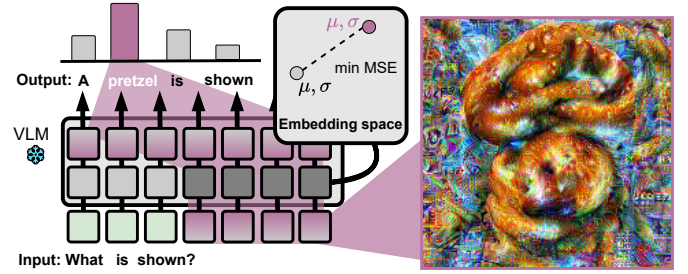


Fig. 1: **Multimodal Inversion for Model Interpretation and Conceptualization (MIMIC)** synthesizes adversarial visual prompts optimized on VLM text outputs. The synthesized images represent the dominant visual features associated with semantic concepts.

We validate the effectiveness of the synthesized images using a diverse set of evaluation metrics that capture classification accuracy, semantic alignment with textual prompts, perceptual similarity to real images, and distributional alignment.

Our contributions are as follows: i) We propose a model inversion objective that can optimize adversarial prompts from varying-length text outputs. ii) We introduce MIMIC, a general approach for inverting VLMs, which, to the best of our knowledge, is the first attempt at synthesizing the conceptual representations of vision-language generative models. iii) We show that MIMIC can invert VLM concepts from text outputs of different lengths, synthesizing high-fidelity images.

II. RELATED WORK

Feature attribution methods have been used to localize feature relevance within inputs. A set of methods is based on Class Activation Maps (CAM) [7, 12, 13], which backpropagate the local activations of class-relevant regions in vision models. Other approaches have been based on pixel-level attributions, such as Layer-wise Relevance Propagation [14], DeepLIFT [15], and Integrated Gradients [8] to propagate relevance or gradient-based signals backwards through the network. Although attribution methods are widely used to explain CNN/ViT-based models for supervised tasks such as classification, detection, or regression, they cannot be directly applied to autoregressive multimodal models. In contrast to these approaches that localize feature attributions for classification, we offer a general approach to visualize internal representations of encoded visual concepts learned by VLMs.

Optimization Objective	Accuracy \uparrow		IS $_{\infty}$ \uparrow			FID $_{\infty}$ \downarrow	IS \uparrow	FID \downarrow	LPIPS \downarrow	CLIPScore \uparrow
	Top-1	Top-5	\mathcal{R}_V	InceptionV3	MobileNetV2					
<i>Partial objectives</i>										
Baseline (\mathcal{L}_{SCE})	0.0	0.0	1.06	1.11	1.10	345.17	1.46	404.56	1.35	23.54
+ Base Feature Loss (\mathcal{L}_{base})	1.66	35.83	1.28	1.55	1.43	299.29	2.85	352.29	1.00	25.76
+Patch Regularizer \mathcal{R}_{patch}	15.83	56.66	1.45	2.32	1.71	280.65	3.88	286.22	0.95	27.21
+Prior Regularizer \mathcal{R}_{prior}	<u>40.00</u>	69.16	<u>1.77</u>	2.59	2.64	253.52	<u>4.26</u>	<u>246.74</u>	0.87	27.67
+Feat. Dist. Regularizer \mathcal{R}_V	30.83	53.33	1.53	<u>3.01</u>	<u>3.67</u>	<u>280.20</u>	3.78	330.84	0.77	25.46
Aggregated Objective	41.25	<u>62.91</u>	2.05	4.25	4.54	227.42	4.91	212.37	<u>0.86</u>	<u>27.42</u>

TABLE I: **Image and semantic quality** across \mathcal{R}_V top-1/5 accuracy, IS $_{\infty}$ across three standardized classification models [30–32], FID $_{\infty}$, IS, LPIPS, and CLIPScore. The aggregated objective yields the best overall performance, while each component improves across semantic, perceptual, and distributional metrics. Best results are in **bold** and second best are underlined.

down. We define an adapted CE loss \mathcal{L}_{SCE} given the token index with the highest logit for [target]:

$$\mathcal{L}_{SCE}(\hat{\mathbf{y}}) = -\sum \mathbb{1}(\text{sg}(\hat{\mathbf{y}}), [\text{target}]) \log(\hat{\mathbf{y}}), \quad (1)$$

where $\mathbb{1}(\text{sg}(\hat{\mathbf{y}}), [\text{target}])$ is the indicator function given index of token [target], stop gradient $\text{sg}(\hat{\mathbf{y}})$, and maximum sequence length $|\hat{\mathbf{y}}|$.

Base Feature Loss. To align synthesized images with the internal representations of the vision encoder $\hat{\mathbf{z}}_l = \mathcal{E}_{\theta_e}(\hat{\mathbf{v}}, l)$, we record mean and variance from real [target] images given $\theta_{e,l}$ weights, across $l \in \Lambda = \{1, \dots, L\}$ layers:

$$\mathcal{L}_{base} = \sum_{l \in \Lambda} \left(\|\mu(\hat{\mathbf{z}}_l, \theta) - \mu(\bar{\mathbf{Z}}_l)\|_2^2 + \|\sigma(\hat{\mathbf{z}}_l, \theta) - \sigma(\bar{\mathbf{Z}}_l)\|_2^2 \right) \quad (2)$$

where Λ denotes the set of chosen layers and $\bar{\mathbf{Z}}_l$ are the averaged embeddings of real [target] images at layer l .

Triplet Feature Regularizer. As VLMs encode multimodal inputs over large and complex feature spaces, we improve the optimization objective by including three regularizers from seminal vision-only (classification) model inversion methods [16–18]. We use \mathcal{R}_{patch} to smooth color transitions across ViT patch boundaries and improve the overall homogeneity of patches in the synthesized images. Our second regularizer \mathcal{R}_{prior} is defined as a combination of image priors. It includes total L1/2 variation \mathcal{R}_{TV_1} and \mathcal{R}_{TV_2} for spatial smoothness and noise reduction, along with ℓ_2 -norm penalty \mathcal{R}_{l_2} to constrain the overall dynamic range:

$$\mathcal{R}_{prior}(\hat{\mathbf{v}}) = \alpha_1 \mathcal{R}_{TV_1}(\hat{\mathbf{v}}) + \alpha_2 \mathcal{R}_{TV_2}(\hat{\mathbf{v}}) + \alpha_3 \mathcal{R}_{l_2}(\hat{\mathbf{v}}) \quad (3)$$

Our final regularizer \mathcal{R}_V constrains embeddings towards known BN feature distribution statistics from an additional domain-specific verifier network \mathcal{F} trained on dataset \mathcal{V} . From F we obtain $\mathbb{E}[\mu_k(\mathcal{F}(\{\mathbf{v}; \mathcal{V}\})), \sigma_k(\mathcal{F}(\{\mathbf{v}; \mathcal{V}\}))]$ and calculate the l_2 distance to $\mu_k(\mathcal{F}(\hat{\mathbf{v}})), \sigma_k(\mathcal{F}(\hat{\mathbf{v}}))$ across $k \in N$ BN layers. The aggregated regularizer $\mathcal{R}(\hat{\mathbf{v}})$ is defined as:

$$\mathcal{R}(\hat{\mathbf{v}}) = \beta_1 \mathcal{R}_V(\hat{\mathbf{v}}) + \beta_2 \mathcal{R}_{patch}(\hat{\mathbf{v}}) + \mathcal{R}_{prior}(\hat{\mathbf{v}}) \quad (4)$$

where $\beta_1, \beta_2, \alpha_1, \alpha_2, \alpha_3$ are scaling factors.

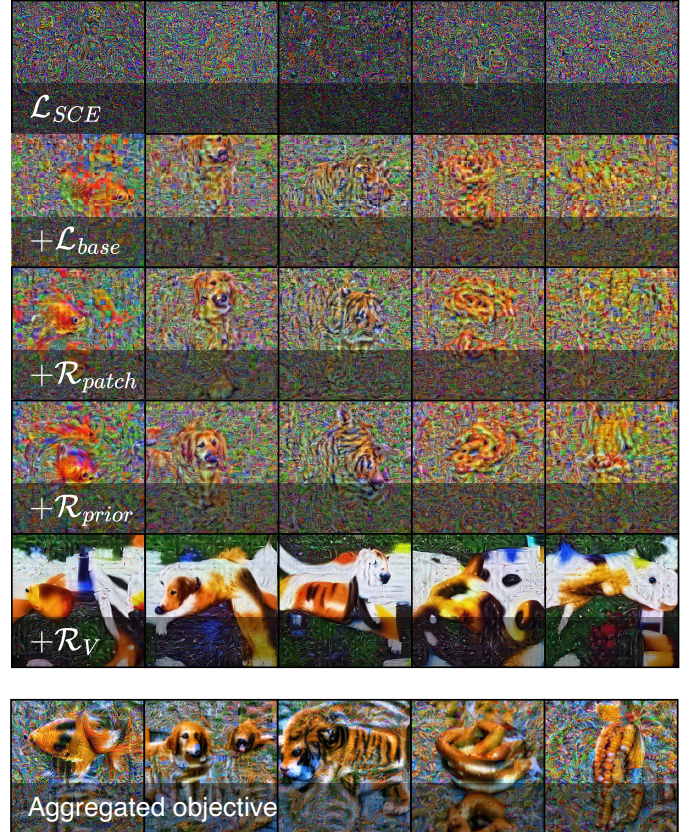


Fig. 3: **Synthesized concepts with different optimization settings** for goldfish, golden retriever, tiger, pretzel, and corn. Each row shows outputs generated using a combination of optimization objectives.

Aggregated Objective. Our final combined optimization objective is backpropagated iteratively to update $\hat{\mathbf{v}}$ over iterative steps, e.g. for $i \rightarrow i + 1$:

$$\hat{\mathbf{v}}_{i+1} = \min_{\hat{\mathbf{v}}_i} \gamma_1 \mathcal{L}_{SCE}(s(\Phi_{\theta_\phi}([\mathcal{G}(\mathbf{t}), \mathcal{E}_{\theta_e}(\hat{\mathbf{v}})]))) + \gamma_2 \mathcal{L}_{base} + \mathcal{R}(\hat{\mathbf{v}}) \quad (5)$$

where it combines (1) and (2) losses and the regularizers from (4) and γ_1, γ_2 with scaling factors. The final objective defines the inversion method that makes internal representations of VLMs visually interpretable through inversion.

Length	BLEU \uparrow	METEOR \uparrow	ROUGE-L \uparrow
$ \hat{y} = 4$	0.749	0.259	0.750
$ \hat{y} = 5$	0.799	0.396	0.800
$ \hat{y} = 7$	0.857	0.422	0.857

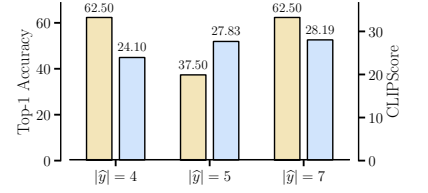
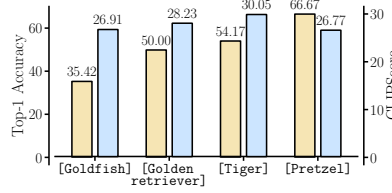


TABLE II: VLM target to predicted text scores across text similarity metrics (BLEU, METEOR, ROUGE-L) with varied target length. Fig. 4: Top-1 accuracy (yellow) and CLIPScore (blue) across different synthesized concepts. Fig. 5: Top-1 accuracy (yellow) and CLIPScore (blue) for target [goldfish] across output lengths.

IV. RESULTS

Model Details We invert LLaVA-1.5 [33] that consists of a CLIP ViT-L/14 [34] vision encoder and a LLaMA-3-8B-Instruct [35] language model. Model parameters remain frozen and the updatable input $\hat{v} \in \mathbb{R}^{3 \times 336 \times 336}$ initialized from a Gaussian distribution $\hat{v} \sim \mathcal{N}(0, 1)$ includes the only updatable parameters. We compute \mathcal{L}_{base} from ImageNet [22].

Implementation Details We perform a grid search over hyperparameters $\{a_1, a_2, a_3, \beta_1, \beta_2, \gamma_1, \gamma_2\}$ per concept, and use [30] for \mathcal{R}_V . We run inversion for 5000 iterations with Adam and fix the random seed $\in \{0, 1, 2\}$ for reproducibility. **Evaluation Metrics.** Quantitative results for each concept reported are obtained from 24 runs for a total of 120 synthesized images. We evaluate the image and semantic quality using top-1 and top-5 classification accuracy [32], perceptual similarity [36], semantic alignment [37], and generative quality [38, 39] metrics. To assess robustness in low-sample scenarios, we also report FID_∞ and IS_∞ [40]. We optimize reconstructions using fixed-format target sentences of varying lengths and evaluate the predicted concepts \hat{y} using BLEU [41], METEOR [42], and ROUGE-L [43] scores across target lengths $|\hat{y}| \in \{4, 5, 7\}$ to assess the impact of textual variability on generation and reconstruction quality.

Baseline results of our method’s performance across configurations are shown in Table I. The aggregated objective achieves a balance across metrics, with 41.25% Top-1 accuracy, 227.42 FID, and 4.91 IS. Structure-based regularizers \mathcal{R}_{patch} and \mathcal{R}_{prior} show the biggest improvement across image quality metrics (IS_∞ , FID_∞). Similarly, \mathcal{L}_{base} and \mathcal{R}_V affect primarily semantic metrics, such as top-1/5 accuracy and CLIPScore.

Qualitative examples across configurations shown in Fig. 3. The trends observed align with quantitative metrics in Table I, with each objective component shaping semantic fidelity and visual structure. \mathcal{R}_{patch} and \mathcal{R}_{prior} improve alignment and enhance smoothness of objects. Both \mathcal{L}_{base} and \mathcal{R}_V optimize towards known distributions of features.

Semantic results of top-1 and CLIPScores across concepts are reported in Fig. 4. In general, both scores only show moderate variations across concepts. Synthesized images of [pretzel] are shown to have the highest top-1 \mathcal{R}_V accuracy while [tiger] has the highest CLIPScore. Table II report language-based similarity between [target] and \hat{y} . The results show that longer target texts yield higher alignment, as suggested by improvements in BLEU, METEOR,

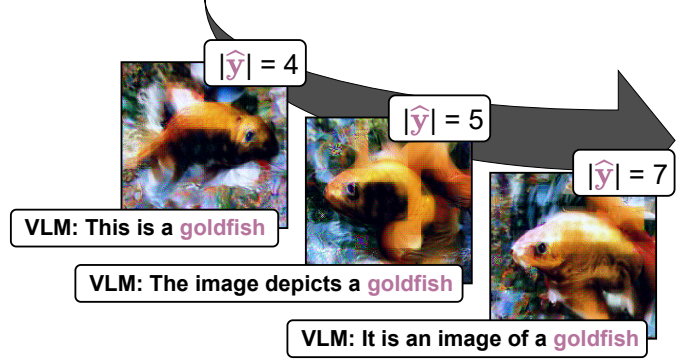


Fig. 6: Target length $|\hat{y}|$ ablations for target concept [goldfish]. Little variance in the synthesized image quality is shown across target lengths.

and ROUGE-L scores due to better lexical and structural conformity with the template. As shown in Fig. 5, synthesized images remain visually consistent across different lengths, indicating that text supervision primarily affects the language output, with a limited impact on visual reconstruction. Further qualitative results in Fig. 6 further demonstrate that object structures and features remain of high fidelity across $|\hat{y}|$.

V. CONCLUSION

In this paper, we propose MIMIC, a framework for synthesizing visual concepts of VLMs. By combining an adapted cross-entropy loss, a base feature loss from ViT activations, and a patch prior regularizer, we recovered semantically aligned and structurally coherent concepts. Our findings contribute to VLM interpretability by showing that rich, visual representations can be extracted through inversion to reveal semantic structure, spatial layout, and low-level texture that VLM models store in ViT’s MLP layers. As future work, we plan to analyze how attention layers encode concept-specific signals and investigate how scaling individual layers affects inversion quality. Additionally, using a larger set of real images to extract target statistics may help guide reconstructions toward more realistic and natural outputs.

REFERENCES

- [1] Yu-Neng Chuang, Guanchu Wang, et al., “Faithlm: Towards faithful explanations for large language models,” *arxiv:2402.04678*, 2024.

- [2] Haozhe Chen, Carl Vondrick, and Chengzhi Mao, “Selfie: Self-interpretation of large language model embeddings,” in *ICML*, 2024.
- [3] Asma Ghandeharioun, Avi Caciularu, et al., “Patchscopes: A unifying framework for inspecting hidden representations of language models,” in *ICML*, 2024.
- [4] Roger Grosse, Juhan Bae, et al., “Studying large language model generalization with influence functions,” *arxiv:2308.03296*, 2023.
- [5] Kevin Meng, David Bau, et al., “Locating and editing factual associations in gpt,” in *NeurIPS*, 2023.
- [6] Finale Doshi-Velez and Been Kim, “Towards a rigorous science of interpretable machine learning,” *arxiv:1702.08608*, 2017.
- [7] Ramprasaath R Selvaraju, Michael Cogswell, et al., “Grad-cam: Visual explanations from deep networks via gradient-based localization,” in *ICCV*, 2017.
- [8] Mukund Sundararajan, Ankur Taly, and Qiqi Yan, “Axiomatic attribution for deep networks,” in *ICML*, 2017.
- [9] Maithra Raghu, Thomas Unterthiner, et al., “Do vision transformers see like convolutional neural networks?,” in *NeurIPS*, 2021.
- [10] Chenyang Zhao, Kun Wang, et al., “Grad-eclip: Gradient-based visual and textual explanations for clip,” in *ICML*, 2024.
- [11] Michal Golovanevsky, William Rudman, et al., “What do vlms notice? a mechanistic interpretability pipeline for gaussian-noise-free text-image corruption and evaluation,” in *ACL*, 2025.
- [12] Bolei Zhou, Aditya Khosla, et al., “Learning deep features for discriminative localization,” in *CVPR*, 2016.
- [13] Haofan Wang, Zifan Wang, et al., “Score-cam: Score-weighted visual explanations for convolutional neural networks,” in *CVPRw*, 2020.
- [14] Sebastian Bach, Alexander Binder, et al., “On pixel-wise explanations for non-linear classifier decisions by layer-wise relevance propagation,” *PLOS ONE*, 2015.
- [15] Avanti Shrikumar, Peyton Greenside, and Anshul Kundaje, “Learning important features through propagating activation differences,” in *ICML*, 2017.
- [16] Hongxu Yin, Pavlo Molchanov, et al., “Dreaming to distill: Data-free knowledge transfer via deepinversion,” in *CVPR*, 2020.
- [17] Ali Hatamizadeh, Hongxu Yin, et al., “Gradvit: Gradient inversion of vision transformers,” in *CVPR*, 2022.
- [18] Amin Ghiasi, Hamid Kazemi, et al., “Plug-in inversion: Model-agnostic inversion for vision with data augmentations,” in *ICML*, 2022.
- [19] Alexandros Stergiou, “The mind’s eye: Visualizing class-agnostic features of cnns,” in *ICIP*, 2021.
- [20] Jason Yosinski, Jeff Clune, et al., “Understanding neural networks through deep visualization,” in *ICMLw*, 2015.
- [21] Anh Nguyen, Jeff Clune, et al., “Plug & play generative networks: Conditional iterative generation of images in latent space,” in *CVPR*, 2017.
- [22] Jia Deng, Wei Dong, et al., “Imagenet: A large-scale hierarchical image database,” in *CVPR*, 2009.
- [23] Thomas Fel, Agustin Picard, et al., “Craft: Concept recursive activation factorization for explainability,” in *CVPR*, 2023.
- [24] Harrish Thasarathan, Julian Forsyth, et al., “Universal sparse autoencoders: Interpretable cross-model concept alignment,” in *ICML*, 2025.
- [25] Edward J Hu, Yelong Shen, et al., “Lora: Low-rank adaptation of large language models,” *ICLR*, 2022.
- [26] Yossi Gandelsman, Alexei A. Efros, and Jacob Steinhardt, “Interpreting the second-order effects of neurons in clip,” in *ICLR*, 2025.
- [27] Mingxu Tao, Quzhe Huang, et al., “Probing multimodal large language models for global and local semantic representations,” in *LREC-COLING*, 2024.
- [28] Tuomas Oikarinen and Tsui-Wei Weng, “Linear explanations for individual neurons,” in *ICML*, 2024.
- [29] Teresa Dorszewski, Lenka Tětková, et al., “From colors to classes: Emergence of concepts in vision transformers,” *arxiv:2503.24071*, 2025.
- [30] Kaiming He, Xiangyu Zhang, et al., “Deep residual learning for image recognition,” in *CVPR*, 2016.
- [31] Christian Szegedy, Vincent Vanhoucke, et al., “Rethinking the inception architecture for computer vision,” in *CVPR*, 2016.
- [32] Mark Sandler, Andrew Howard, et al., “Mobilenetv2: Inverted residuals and linear bottlenecks,” in *CVPR*, 2018.
- [33] Haotian Liu, Chunyuan Li, et al., “Improved baselines with visual instruction tuning,” in *CVPR*, 2024.
- [34] Alec Radford, Jong Wook Kim, et al., “Learning transferable visual models from natural language supervision,” in *ICML*, 2021.
- [35] AI@Meta, “Llama 3 model card,” 2024.
- [36] Richard Zhang, Phillip Isola, et al., “The unreasonable effectiveness of deep features as a perceptual metric,” in *CVPR*, 2018.
- [37] Jack Hessel, Ari Holtzman, et al., “Clipscore: A reference-free evaluation metric for image captioning,” in *EMNLP*, 2022.
- [38] Martin Heusel, Hubert Ramsauer, Thomas Unterthiner, Bernhard Nessler, and Sepp Hochreiter, “Gans trained by a two time-scale update rule converge to a local nash equilibrium,” *NeurIPS*, 2017.
- [39] Tim Salimans, Ian Goodfellow, et al., “Improved techniques for training gans,” *NeurIPS*, 2016.
- [40] Min Chong and David Forsyth, “Effectively unbiased fid inception score and where to find them,” in *CVPR*, 2020.
- [41] Kishore Papineni, Salim Roukos, et al., “Bleu: a method for automatic evaluation of machine translation,” in *ACL*, 2002.
- [42] Satyanjeev Banerjee and Alon Lavie, “Meteor: An automatic metric for mt evaluation with improved correlation with human judgments,” in *ACLw*, 2005.
- [43] Lin Chin-Yew, “Rouge: A package for automatic evaluation of summaries,” in *TSBOW*, 2004.

APPENDIX A ViT INVERSION WITH MIMIC

In addition to VLMs, we apply *MIMIC* on Vision Transformers (ViTs) used on image classification objectives. For these experiments, we initialize an updatable input \hat{v} as in Sec. III. The synthesized image is then passed through the frozen ViT model $f(\cdot)$ to obtain class logits $\hat{y} = f(\hat{v})$.

Objective. For ViT inversion, we adapt the general objective in Eq. 5 to a classification setting. Specifically, we replace the adapted cross-entropy loss \mathcal{L}_{SCE} with a standard cross-entropy loss \mathcal{L}_{CE} applied to the logits \hat{y} and the target label y . The base feature loss \mathcal{L}_{base} and the regularization term \mathcal{R} remain unchanged.

$$\hat{v}_{i+1} = \min_{\hat{v}_i} \gamma_1 \mathcal{L}_{CE}(f(\hat{v}), y) + \gamma_2 \mathcal{L}_{base} + \mathcal{R}(\hat{v}) \quad (\text{A-1})$$

By iteratively updating \hat{v} , the optimization objective in Eq. A-1 produces reconstructions that the model confidently associates with the target class. We use activations from the final LayerNorm, MLP blocks, and patch embedding layers of the ViT as feature targets for \mathcal{L}_{base} loss. This setup allows us to examine how well ViTs alone capture and express class-specific features during inversion.

A. Implementation Details

We evaluate our modified methodology on ViT-B/16 [1]. Starting from Gaussian noise, we iteratively update synthetic images to match the internal representations of the target class *dog* from the Oxford-IIIT Pet dataset [2].

We run the inversion for 3000 iterations with a batch size of 32, using the Adam optimizer and a cosine learning rate schedule. A grid search over loss weights gives stable reconstructions with $\gamma_1 = 0.3$, $\gamma_2 = 5 \times 10^{-5}$, $\beta_1 = 1 \times 10^{-4}$, $\beta_2 = 4 \times 10^{-3}$, $\alpha_1 = 3 \times 10^{-4}$, $\alpha_2 = 1 \times 10^{-4}$, $\alpha_3 = 1 \times 10^{-5}$.

B. Results

A pretrained MobileNetV2 verifier evaluates the reconstructed images. The synthesized images achieve 53.13% top-1 and 68.75% top-5 accuracy on the verifier, indicating that the images preserve semantically meaningful structure. By around 2200 iterations, reconstructions already capture coherent features such as fur texture, nose shape, and the general silhouette of dogs, although some artifacts and smoothing effects remain. Fig. A-1 shows the synthesized images that confirm our inversion pipeline extracts interpretable visual features from ViT embeddings.

APPENDIX B ABLATION STUDIES

A. Impact of Loss Components and Regularizers

To study the contribution of each component in our inversion objective, we perform systematic ablations where we enable one loss or regularizer at a time and examine its effect on reconstruction quality (Fig. 3). Starting from the baseline \mathcal{L}_{SCE} , we progressively add the \mathcal{L}_{base} , \mathcal{R}_{patch} , \mathcal{R}_{prior} and \mathcal{R}_V to reveal how each term affects semantic alignment,

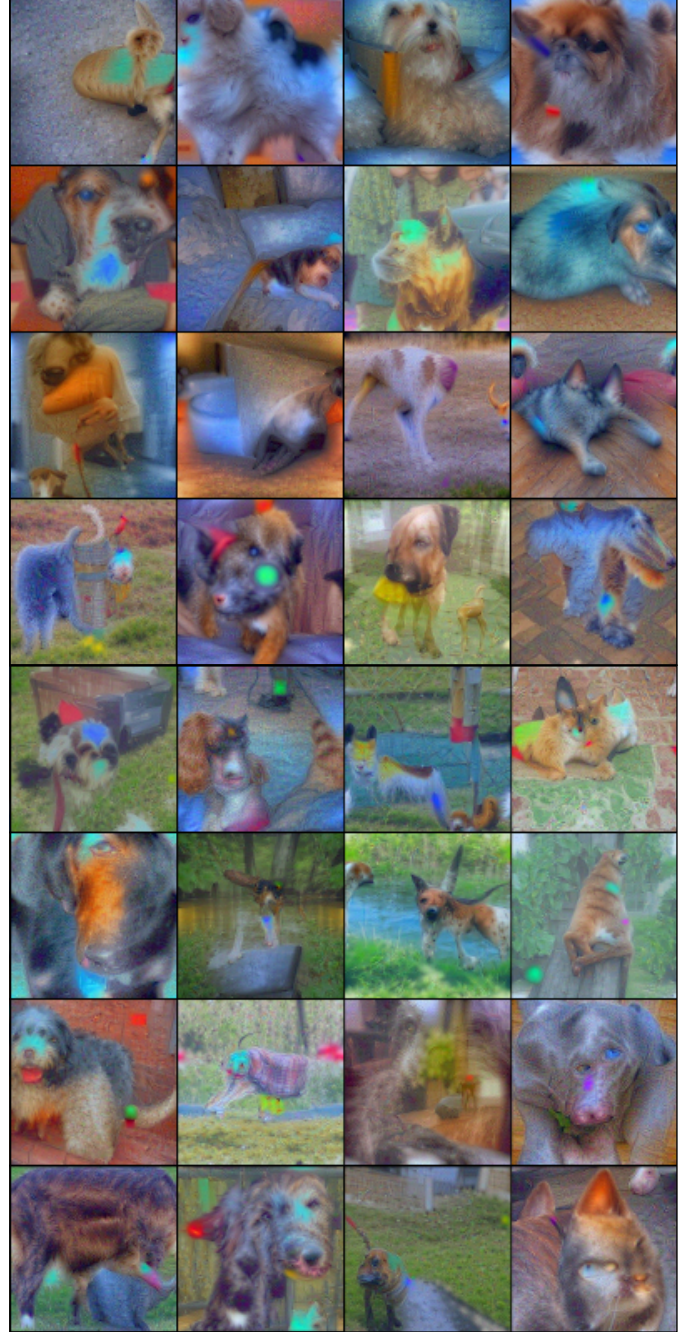


Fig. A-1: Example reconstructed images (batch size = 32) optimized from random noise using our inversion framework applied to ViT-B/16. The images correspond to the class *dog*.

spatial structure, texture smoothness, and overall fidelity. For the ablation experiments, we use the default scale of 1.0 for all loss and regularizer terms. Here, we explore in detail how each loss and regularization component contributes to the overall reconstruction quality.

Adapted CE loss (\mathcal{L}_{SCE}) alone results in highly noisy and structurally incoherent reconstructions across all concepts, as shown in Fig. 3. The likely cause is the limited influence of vision on language in VLMs like LLaVA [33]. In these models,

the CLIP encoder and language model are only loosely aligned at the feature level. This leads to minimal feedback from text to visual features.

Base feature loss (\mathcal{L}_{base}) significantly improves semantic structure by aligning to ViT encoding’s statistics. For example, in Fig. 3, the tiger class exhibits recognizable striped textures similalry, the signature body shape is synthesized for goldfish. However, these images remain spatially inconsistent, with features appearing disorganized or fragmented. This effect can be attributed to the non-local positional encoding of ViT, which lacks inductive biases for preserving spatial layout.

Patch regularizer (\mathcal{R}_{patch}) improves spatial coherence by promoting continuity across patch boundaries. This is most effective in classes with strong localized structures. For example, for golden retriever, facial features like eyes and ears become more aligned. Nevertheless, grid-like artifacts persist, and while positional layout improves, the images still lack perceptual smoothness. Table I confirms the improved structural alignment, with Top-1 accuracy reaching 15.83%, Top-5 accuracy 56.66%, and CLIPScore rising to 27.21, though the visual quality remains limited by residual grid artifacts.

Pixel-based prior (\mathcal{R}_{prior}) including total variation ($\mathcal{R}_{TV_1}, \mathcal{R}_{TV_2}$) and ℓ_2 -norm regularization (\mathcal{R}_{ℓ_2}), further enhances naturalness by suppressing high-frequency noise and encouraging low-level smoothness. These priors are particularly effective for more abstract or texture-heavy concepts like pretzel, which sees the highest top-1 accuracy under this configuration. However, if not properly balanced, these priors can dominate the optimization objective, particularly in the case of the ℓ_2 -norm, where the large magnitude of unnormalized values can dominate other loss components and lead to desaturated or grayed reconstructions.

Feature distribution regularizer (\mathcal{R}_V) sharpens overall textures by matching the global statistics from CNN’s BN layers. However, it often interferes with class-specific structure when overly weighted. For instance, goldfish reconstructions exhibit enhanced surface detail but also display less coherent structure and ambiguous shape, as seen in Fig. 3. We also observe that images across different classes tend to share similar color tones and texture patterns. This suggests that while \mathcal{R}_V encourages alignment with CNN statistics, it may compete with the ViT-guided \mathcal{L}_{base} , leading to visually sharper and smoother reconstructions that lack clear class-specific features.

B. Base Feature Loss (KL Divergence Variant)

We additionally explore a variant of the base feature loss that uses Kullback–Leibler (KL) divergence instead of the ℓ_2 -norm for matching layer statistics. Similar to our standard formulation in Sec. III, we compute the mean and variance of intermediate activations $\hat{\mathbf{z}}_l$ from the vision encoder internal representations of the vision encoder \mathcal{E}_{θ_e} , but instead of directly minimizing their squared differences, we align them over their distributions \mathcal{N} . Specifically, for each selected layer $l \in \Lambda$, we define:

[target] concept	ℓ_2 Loss	KL Divergence Loss
Goldfish	26.91	32.09
Golden Retriever	28.23	29.93
Tiger	30.05	30.04
Pretzel	26.77	28.90
Corn	27.00	30.79

TABLE B-I: CLIPScore comparison between using ℓ_2 -based and KL-divergence-based base feature loss for different [target].

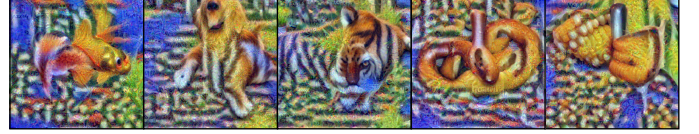


Fig. B-1: Synthesized images for goldfish, golden retriever, tiger, pretzel, and corn using KL-divergence for base feature loss, showing improved alignment of reconstructed features.

$$\mathcal{L}_{base} = \sum_{l \in \Lambda} \text{KL} \left(\mathcal{N} \left(\mu(\hat{\mathbf{z}}_l, \theta), \sigma^2(\hat{\mathbf{z}}_l, \theta) \right) \parallel \mathcal{N} \left(\mu(\bar{\mathbf{Z}}_l), \sigma^2(\bar{\mathbf{Z}}_l) \right) \right) \quad (\text{B-1})$$

where Λ denotes the set of chosen layers and $\bar{\mathbf{Z}}_l$ are the averaged embeddings of real [target] images at layer l . Eq. B-1 encourages the reconstructed image to align with the distribution of the vision encoder’s internal features, potentially capturing richer structure during inversion.

1) *Implementation Details:* We follow the same experimental configuration as in the main inversion setup, with two modifications: the optimization is performed for 3000 iterations, and the scaling factors $\alpha_1, \alpha_2, \alpha_3, \beta_2, \gamma_1$, and γ_2 are set to 1.0 while β_1 is set to 1×10^{-4} . All other hyperparameters and training settings remain unchanged.

2) *Results:* As shown in Fig. B-1, replacing the ℓ_2 -based base feature loss with a KL-divergence formulation produces synthesized images that are less noisy and capture more distinctive semantic details, such as fine textures and clearer object boundaries (e.g., the fins of the goldfish, the body structure of the retriever, and the braided form of the pretzel). Table B-I further supports the qualitative improvement by the CLIPScore comparison, where the KL-based loss consistently yields stronger alignment with target concepts. These results highlight that modeling full feature distributions can provide an informative alternative to directly matching mean and variance, leading to outputs that better preserve the semantic content of the base model’s internal representations.

Although the KL-divergence variant gives higher CLIP-Scores and sharper images with default scaling factors α, β, γ . We keep the ℓ_2 -based \mathcal{L}_{base} as default to remain consistent with DeepInversion [16] and GradViT [17] and avoid the additional computational cost introduced by distributional KL matching. Consequently, KL-based results are reported only as an ablation.

Prompt: Name the object in the image in this format: It is a <object>

Target: It is a goldfish

Predicted: It is a fishfish

Prompt: Name the object in the image in this format: The image depicts a <object>

Target: The image depicts a goldfish

Predicted: The image depicts a fishfish

Prompt: Name the object in the image in this format: It is an image of a <object>

Target: It is an image of a goldfish

Predicted: It is an image of a fishfish

Fig. B-2: Text outputs with varied target length for the goldfish concept, showing prompts, target texts, and predicted responses.

Prompt: Describe the content of the image.

Target: The image shows a goldfish with glossy orange scales, bulging eyes, and wide, delicate fins.

Predicted: The image features a groupfish swimming a orange scales swimming swimmingging eyes, and a fins open fins swimming

Prompt: Describe the content of the image.

Target: The image shows a bright orange fish with a round body, shiny scales, and fan-shaped fins.

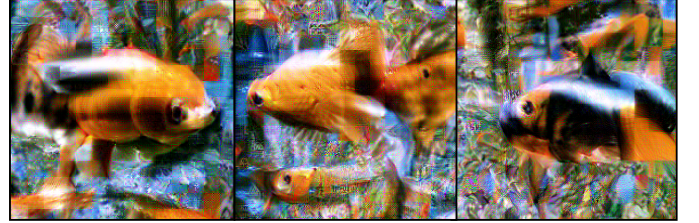
Predicted: The image features a groupfish swimming a orange scales swimming swimmingging eyes, and a fins open fins swimming

Fig. B-3: Text outputs with descriptive target text for the [goldfish] concept, showing prompts, target texts, and predicted responses.

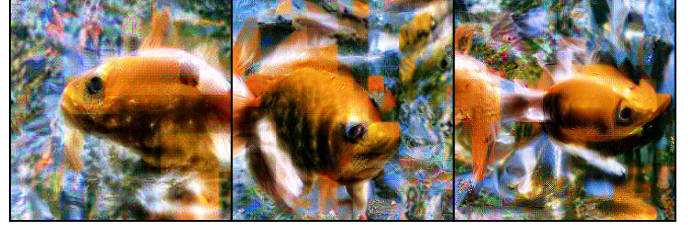
C. Effect of Textual Variations

To assess the role of textual supervision in guiding visual inversion, we analyze two forms of prompt variation: sentence length and descriptive phrasing. These ablations allow us to evaluate whether the structure or richness of the target prompt influences the fidelity of reconstructions. We focus on the goldfish category and reconstruct 8 images per setting using the same optimization configuration as in our main experiments.

1) *Varying target length:* We evaluate the impact of [target] length using fixed templates with $|\hat{y}| \in \{4, 5, 7\}$. Templates used are shown in Fig. B-2 and the corresponding quantitative and qualitative results are shown in Table II and Figs. 5 and 6. Despite variation in length, the reconstructed images remain visually consistent, and the predicted outputs preserve the core semantic content. BLEU and METEOR scores increase slightly with longer prompts, reflecting better lexical overlap. More notably, CLIPScore improves from 24.1 to 28.2, indicating stronger semantic alignment between the synthesized image and the textual prediction. These findings suggest that while prompt length introduces only minor changes in visual appearance, it may still influence the alignment between modalities, particularly as captured by image-text retrieval metrics.



(a) D_1 : The image shows a goldfish with glossy orange scales, bulging eyes, and wide, delicate fins.



(b) D_2 : The image shows a bright orange fish with a round body, shiny scales, and fan-shaped fins.

Fig. B-4: Synthesized images for [goldfish] concept using textual supervision from two descriptions D_1 and D_2 .

2) *Varying target description:* We further examine the effect of using more natural, free-form descriptions from the templates shown in Fig. B-3. Table B-II compares descriptions D_1 (Fig. B-4a) and D_2 (Fig. B-4b) with differing lexical structures. We observe that text similarity metrics such as BLEU and ROUGE-L are slightly lower than those observed in the fixed-length targets. Despite this, we observe notable gains in CLIPScore and Top-1 accuracy for both descriptions (Fig. B-5), indicating stronger alignment between the synthesized image and its semantic label. The corresponding images in Fig. B-4 appear with sharper color. These results suggest that while lexical alignment may decrease, descriptive prompts may provide more effective guidance during optimization.

These findings indicate that textual supervision influences inversion more than it appears visually, and that prompt design plays a meaningful role in guiding during inversion of vision-language models.

Description	BLEU \uparrow	METEOR \uparrow	ROUGE-L \uparrow
D_1	0.444	0.215	0.493
D_2	0.521	0.218	0.557

TABLE B-II: **Text similarity scores** for reference descriptions D_1 (Fig. B-4a) and D_2 (Fig. B-4b) for the [goldfish] concept.

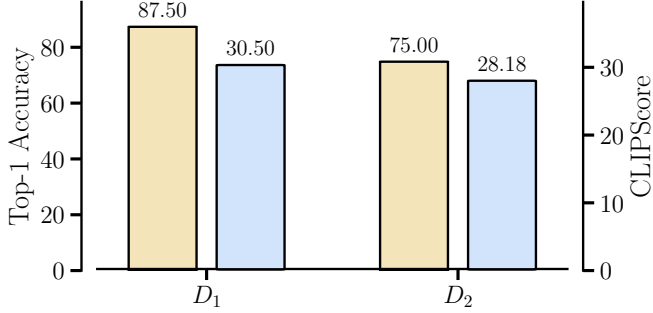


Fig. B-5: **Top-1 accuracy (yellow) and CLIPScore (blue)** for goldfish class across D_1 and D_2 descriptions.

APPENDIX REFERENCES

- [1] A. Dosovitskiy et al., “An Image is Worth 16x16 Words: Transformers for Image Recognition at Scale,” *arXiv:2010.11929*, 2020.
- [2] O. M. Parkhi, A. Vedaldi, A. Zisserman, and C. V. Jawahar, “Cats and dogs,” in *IEEE Xplore*, 2012.